13th ewtec 2019 Proceedings of the 13th European Wave and Tidal Energy Conference 1-6 Sept 2019, Naples, Italy

Hydrodynamics of tidal turbine blades

Gabriel T. Scarlett and Ignazio M. Viola

Abstract — **Tidal turbines encounter a range of unsteady flow conditions, some of which may induce severe load fluctuations. A rotor's blade can experience stall delay, load hysteresis and dynamic stall. Yet, the range of flow conditions which cause these effects for a full-scale axial-flow turbine are unclear. In this work we carry out a parameter study across a range of flow conditions by modelling root bending moment responses. We show how unsteadiness manifests along the span of the blade, the unsteady phenomena occurring and the conditions which induce the most significant load fluctuations. We find that waves and turbulence are the main sources of unsteadiness, and that extreme waves dominate over extreme turbulence. A yaw misalignment increases the load fluctuations but reduces the maximum peak. Large yaw angles, low tip-speed ratios, and very large waves lead to dynamic stall increasing the mean loads. Conversely, added mass effects mostly attenuate the loadings.**

Keywords—**unsteady hydrodynamics, tidal energy, dynamic stall, wave-induced loading, turbulence-induced loading, fatigue loading.**

I. INTRODUCTION

The ocean is inherently unsteady. Currents, waves, turbulence and the channel boundary layer present a challenging environment in which to deploy a tidal energy harvester. Tidal power generation is approaching a state of commercial readiness [1] with significant projects now underway [2]. Yet, questions remain regarding survivability [3, 4]. To be commercially viable devices must endure up to 25 years in the water without requiring major overhaul or repair.

As a rotor's blade rotates through unsteady flow, large differences in the loads can occur compared to those experienced under steady conditions. A better understanding of the conditions that induce the most significant load fluctuations will improve the design and longevity of the device, which in turn will reduce the levelised cost of tidal energy.

Paper ID number: 1460- Track: THM
This work was supported by the Engineering Physical Sciences Research Council [grant number EP/M508032/1].

G. T. Scarlett is a PhD candidate at the School of Engi- neering, Institute for Energy Systems, The University of Edinburgh, Edinburgh, EH9 3BF (email: G.Scarlett@ed.ac.uk).

I. M. Viola is Senior Lecturer at the School of Engineer- ing, Institute for Energy Systems, The University of Edinburgh, Edinburgh, EH9 3BF (email: I.M.Viola@ed.ac.uk)

The unsteady hydrodynamics of a tidal turbine blade depends on whether the flow is attached to, or separated from its surface. The latter induces moderate load oscillations, whereas the former can elicit significant fluctuations. In attached flow there are two interconnected flow phenomena. The first, known as the circulatory effect, arises when vorticity is shed from the trailing edge. This causes a change in the bound circulation around the foil and a subsequent amplitude reduction and phase lag in the lift response with angle of attack, compared to the quasi-steady value. The second, non-circulatory effect, is the added mass. Dynamic stall manifests when unsteady separation and stall occur resulting in a clockwise hysteresis loop of the lift response with the angle of attack. Lift increases above the static stall angle as stall is delayed to a greater angle, then at a sufficiently large angle of attack a leading edge vortex may form and convect over the surface producing a further increase in lift. Unlike attached unsteady flow, lift fluctuations twice the static value can occur [5]. For a rotor blade the combination of blade rotation, which induces a centrifugal and Coriolis force on the flow, with dynamic stall can produce very large lift amplitudes compared to the non-rotational case [6, 7].

To date, the quantification of the unsteady loads incident to a tidal turbine rotor have been confined to scaled geometries, operating in simplified flows. Whelan *et al*. [8] carried out experiments on a scaled turbine in a towing tank. The turbine was towed at a uniform speed whilst oscillating the external carriage on which it was mounted. This generates oscillations in the rotor plane which are uniform with depth. In an attempt to quantify the circulatory and added mass contributions to the forces, the authors compared measured thrust data with Morrison's equation, which conveniently separates the added mass and drag force. Their study concluded that, for the range of frequencies tested, the added mass contribution was small. Milne *et al*. [9, 10] also carried out towing tank experiments and compared root bending moment measurements with Theodorsen's theory [11] which separates the circulatory and non-circulatory lift response. These results revealed that circulatory effects dominate over added mass effects at low frequencies.

With regard to separated flow, Milne *et al*. [9] determined that, at low tip-speed ratios, the flow was separated over most of the blade span, which for high frequency forcing caused the root bending moment to exceed the quasi-steady value by up to 25%. In a later study, Milne *et al*. [12] identified the key stages of dynamic stall in the root bending moment hysteresis. Gal-

loway *et al*. [13] investigated the effects of a yaw misalignment and waves using a wave tank to generate linear waves. Results were compared with an in house blade-element momentum code, which included a dynamic stall and dynamic inflow correction. The experimental results revealed that the median value of the root bending moment was exceeded by up to 175% during the presence of large waves. The authors concluded that the effect of dynamic stall is limited and, therefore, can be neglected in some cases, despite not making comparison with quasi-steady values. In our recent study we quantified the loads for a full-scale, 1 MW horizontal axes tidal turbine operating in large wave conditions [7]. The loads, moments and power were modelled using measured flow velocity data from the European Marine Energy Center. The study revealed that the significance of dynamic stall depends on how the turbine is operated. When operating at the optimal tip-speed ratio, separation and dynamic stall is confined to the blade root, which is in agreement with Galloway *et al*. [13]. However, reducing the tip-speed ratio led to increased flow separation and dynamic stall, which caused overshoots in the mean root bending moment compare to simple quasi-steady approximation. These latter findings concurs with the experiments of Milne *et al*. [12].

Overall, these past results show that, in some realistic unsteady flow conditions, the flow around the blade is dominated by dynamic stall, and this results in large load peaks and lower energy efficiency. However, there has yet to be a comprehensive study of global and local blade loadings for a broad range of flow conditions. In this paper we explore the different unsteady phenomena occurring along the blade span due to the shear layer, turbulence, waves and a yaw misalignment. Using our recently developed unsteady load model for arbitrary forcing [7], we identify the conditions which elicit the most significant load fluctuations and, for these conditions, how unsteadiness manifests along the span of the blade. We determine which blade section incurs the largest load fluctuations and whether added mass effects are amplifying or attenuating them.

II. TURBINE SPECIFICATION

The dimensions of a 3-bladed, 1 MW tidal turbine representative of the Tidal Generation Ltd. DEEPGEN IV device deployed at the European Marine Energy Center (EMEC) test site during the ReDAPT project are considered. Schematic views of the port and front sides of the turbine are shown in Figure 1. A Cartesian coordinate system is placed at the still water level (SWL). The freestream current velocity is in the x direction, y is the port side direction and z is the vertical coordinate positive above the SWL. A cylindrical coordinate system with origin at the hub describes the radial (r) position along the blade, which extends to the tip ($R = 9$ m), and the azimuthal angle of the blade (ψ), which tracks the position of the blade as it rotates counter-clockwise from the z axis where $\psi = 0$. Also shown are the radius of the hub ($R_h = 1.0$ m), the water depth ($d = 45$m) and the distance from the hub to the SWL ($z_0 = 27$m). The chord (c) and geometrical twist (β_g) distributions

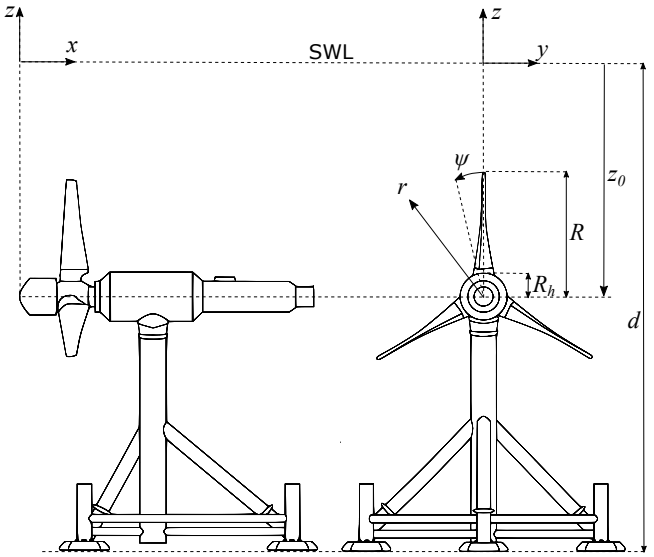

Fig.1. Schematic diagram of the tested tidal turbine.

along the blade span, follow those from Gretton [14]. The blade profile is assumed to comprise of NREL S814 geometries which have a uniform maximum thickness in relation to the chord of 24%.

In a previous study the turbine was found to yield a peak power coefficient $C_P = 0.47$ when operating at a tip-speed ratio ($\lambda = 4.5$). Full details of this study can be found in Scarlett *et al*. [7]

III. HARMONIC LOAD OSCILLATIONS

We investigate attached flow effects analytically for simple harmonic forcing using Theodorsen's theory [11].

Theodorsen provides the unsteady lift coefficient for a flat plate undergoing oscillations in angle of attack (α), pitch or plunge [11]. The solution is given explicitly, but restricted to pure harmonic forcing. Here we assume the forcing is pure α oscillations of the form $\alpha(t) = \bar{\alpha} + \alpha_0 e^{i2\pi ft}$, where $\bar{\alpha}$ is the mean value, α_0 the amplitude, f the forcing frequency and t is time. Theodorsen's solution is then

$$C_L = [i\pi k + 2\pi C(k)]\alpha(t). \tag{1}$$

The first term in Equation 1 is the non-circulatory, added mass effect, and the second term, is the circulatory effect. $C(k)$, which multiplies the circulatory term is Theodorsen's complex transfer function, defined as

$$C(k) = \frac{H_1^{(2)}(k)}{H_1^{(2)}(k) + iH_0^{(2)}(k)}, \tag{2}$$

where $H_v^{(2)} = J_v - iY_v$ is a Hankel function of the second kind; J_v and Y_v are Bessel functions of the first and

second kind respectively; v refers to the order, which in this model takes either the value 0 or 1. The argument k is the reduced frequency, a non-dimensional parameter that is a measure of the unsteadiness. In general, the flow is said to be unsteady if $k > 0.05$, and highly unsteady for $k > 0.2$ [15]. The reduced frequency is defined as

$$k = \frac{\pi f c}{U_r}, \tag{3}$$

where U_r is the relative velocity.

Using Theodorsen's theory we investigate how the lift response varies at a blade section near the tip ($r \approx 0.98R$ and $c \approx 0.8$ m), where the flow is attached. Three values of k are simulated: $k = 0.07$, $k = 0.16$ and $k = 0.31$. Representing a 10 s period wave, a once per revolution, and a twice per revolution forcing, respectively. The turbine is operating at the optimum $\lambda = 4.5$. For each case we assume a moderate forcing $U_r = 7.0$ ms^{-1}, $\alpha_0 = 4^\circ$, and $\bar{\alpha} = 5^\circ$. The results are shown in Figure 2, alongside the quasi-steady value ($2\pi\alpha$) corresponding to $k = 0$, for comparison. We observe that the

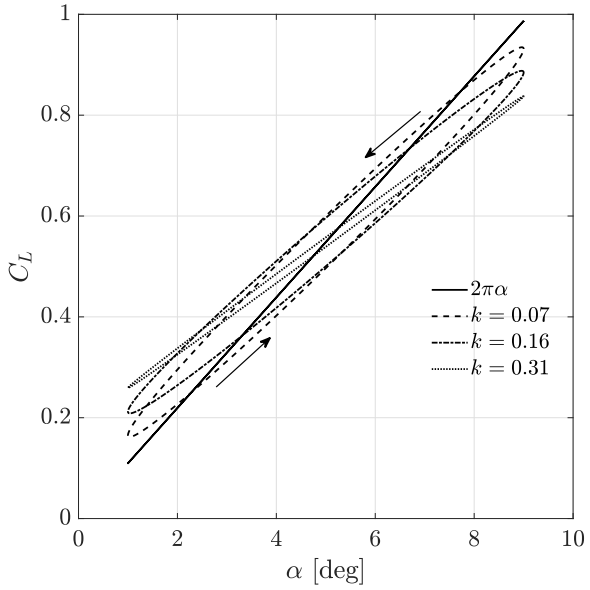

Fig. 2. Unsteady lift coefficient given by Theodorsen for a section near the tip of the blade. The static linear value ($2\pi\alpha$) is shown for comparison.

unsteady responses are counter-clockwise hysteresis in C_L with α, and that there is an amplitude reduction and phase lag compared to the quasi-steady value, which for this k range decreases inversely with k.

Theodorsen's model conveniently separates the circulatory and non-circulatory components, enabling the contribution of each to the total C_L response to be quantified. Defining the normalised lift coefficient amplitude (ζ) as

$$\zeta = \frac{|C_L|}{2\pi|\alpha_0|} = |(F + iG) + i\frac{k}{2}|, \tag{4}$$

where the first and second terms are the circulatory and added mass components respectively, $F = \mathrm{Re}(C(k))$ and $G = \mathrm{Im}(C(k))$. In Figure 3(a) the contribution to ζ is shown for $k \in [0, ..., 4]$. We find that if $k \leq 1.8$ then $\zeta < 1$, however, when $k > 1.8$, the amplitude exceeds the steady value ($\zeta > 1$) and then increases with k, approaching the added mass linear response in the limit. Figure 3(b) shows a magnification of the region $k \in [0, 1]$, which is the range in which a tidal turbine operates. Interestingly in the interval $[0 < k < 0.56]$, added mass dampens the total response. This is because the circulatory and added mass components are combined vectorially. Since tidal turbines mostly operate within this interval, added mass effects are unlikely to become a problem. This is important since it has been suggested [8, 16] that the high density of water might lead to significant added mass effects for tidal turbines. However, this is not the case as long as $k < 0.56$. Conversely, the circulatory response, associated with dynamic inflow, is the significant effect, which concurs with the scale model results of Milne *et al*. [9]. Clearly the observation from Figure 2, that the amplitude reduces inversely with k, are only true inside the interval $[0 < k < 0.56]$. For $k > 0.56$ the relationship inverts.

IV. GLOBAL BLADE RESPONSE TO UN- STEADY FLOW CONDITIONS

In this section we investigate the wide range of unsteady flow conditions which a tidal turbine blade may encounter. Firstly, individual shear, turbulence and wave forcings are considered. These results are used to select combined realistic flows which are further examined. The responses are categorised by the standard deviation of the root bending moment coefficient (C_{M_y}), defined as

$$C_{M_y} = \frac{2M_y}{\pi R^3 \rho U_0^2}, \tag{5}$$

where ρ is the fluid density. Events where the mean root bending moment coefficient exceeds the quasi-steady counterpart ($C_{M_y q.s}$) are identified by isolines of the ratio: $\bar{C}_{M_y}/\bar{C}_{M_y q.s}$, where the overbar indicates the time averaged operator. This will indicate the extent to which dynamic stall is having a global effect.

Simulations are carried out using our unsteady tidal turbine model which is described in detail in Scarlett *et al*. [7], and freely available to download from our GitHub repository [17]. There is a blade-element momentum implementation using the solution method of Ning [18]. The unsteady loads are determined in the time domain for any arbitrary forcing. The model comprises of an attached load model using the time-domain solution of Wagner [19], which is analogous to Theodorsen's frequency-domain solution, and a dynamic stall implementation which is based on the model of Sheng *et al*. [20]. A modification is made to account for rotational augmentation using the model of Lindenburg [21]. It is important to note that the attached flow solution is part of the non-linear dynamic stall solution. When the flow remains attached, the solution tends to

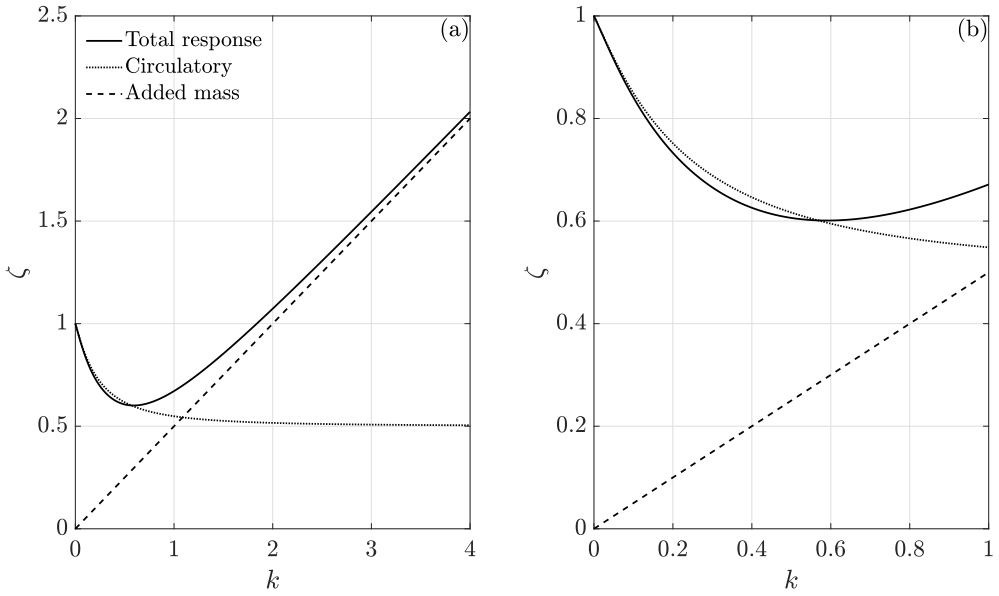

Fig. 3. Normalised amplitude of the total, circulatory and non-circulatory coefficients with reduced frequency for pure angle of attack oscillations.a, full range, b, tidal turbine range.

Theodorsen's solution. However, any arbitrary forcing can be considered. The quasi-steady value is predicted using static wind tunnel measurements of the force coefficients [22].

A. Once per revolution forcing

A once per revolution forcing (1P) due to the rotation of the blade through the shear flow and a yaw misalignment is considered. The shear flow is associated with the tidal channel boundary layer. The horizontal current velocity u_x is non-uniform with depth due to the presence of the bed, which causes a reduction in the velocity profile with depth. At the bed there is no slip ($u_x(-d) = 0$). At the still water level we set $u_x(0) = U_\infty$. The u_x profile is then defined using a power law approximation:

$$u_x = U_\infty \Big(\frac{z+d}{d}\Big)^\nu, \tag{6}$$

for $-d \leq z \leq 0$. In this study $\nu = 1/7$, which was found to be an excellent fit of the time-averaged velocity profile within the depth range of a turbine operating at EMEC [7]. If the turbine is yawed relative to the freestream at a yaw angle (γ) the streamwise velocity is reduced by $\cos(\gamma)$ and a tangential, azimuthally varying component; $u_x \sin(\gamma)\cos(\psi)$ appears. In addition, blade sections downstream relative to the center of the hub, encounter more of the wake, therefore, a greater induced velocity. Conversely, blade sections upstream of the hub, outside of the wake encounter a lower induced velocity. We incorporate this effect into the axial induction factor using the uncoupled approach given by Ning *et al*. [23], which post corrects a after the blade-element momentum algorithm converges for zero yaw. The tangential induction factor remains unchanged. The corrected induction factor is

$$a_\gamma = a\Big(1 + \frac{15\pi}{32}\mu \tan\chi \cos\psi\Big), \tag{7}$$

where χ is the wake skew angle which is approximated as $\chi \approx (0.6a + 1)\gamma$ [24].

A range of 1P inflow conditions, $U_0 \in [1.2, 3.5]$ ms^{-1}, $\lambda \in [3, 7]$ and $\gamma[0, 180^\circ]$ are simulated over 50 rotations. For each flow condition the standard deviation of the root bending moment ($\sigma_{C_{M_y}}$) is predicted. The results displayed in Figure 4 show that, $\sigma_{C_{M_y}}$ increases with γ and the inverse of λ. At low λ, dynamic stall effects the mean loads, even when the only source of unsteadiness is the rotation through the shear layer. This is evident by the 1.00 isoline indicating the boundary where $\bar{C}_{M_y}/\bar{C}_{M_y(q.s)}$ becomes positive for the $\gamma = 0$ case. The range increases to $\lambda \approx 4$ for $\gamma = 40^\circ$, and $\lambda \approx 4.5$ for the largest $\gamma = 50^\circ$ case. However, as γ increases the ratio decreases, with no values above 1.10 occurring for $\gamma > 20^\circ$. At high λ, added mass effects result in lower C_{M_y} compared to the quasi-steady counterpart. However, we found that the ratio is never below 0.95, and hence no isolines of values below unity are displayed.

Thus, at low λ, unsteady conditions will always increase the mean loads compared to a quasi-steady prediction. This is due to the slower rotational speed, which reduces the tangential velocity, which increases α. As α increases along the blade, dynamic stall becomes the dominant loading regime. This has previously been reported for large wave induced loads when operating at lower, sub-optimal values of λ [7]. These results show that the yaw misalignment must be extremely significant to affect the mean loads at the optimal λ.

B. Turbulence forcing

Turbulent velocity fluctuations are synthesised using the von Kármán atmospheric turbulence spectrum [25],

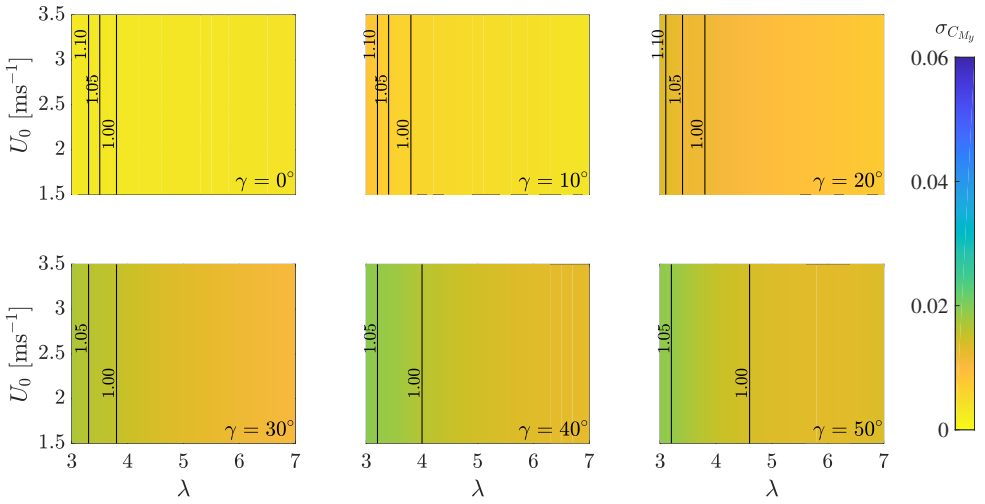

Fig. 4. Filled contour map showing the standard deviation of the root bending moment due to varying current velocity, tip-speed ratio and yaw angle. Solid contour lines show the ratio between the mean root bending moment and the quasi-steady counterpart.

which has widely been used in wind engineering and wind energy research [24]. Recent characterisation studies of the turbulent flow structure at the Sound of Islay ascertained that the von Kármán spectra predicted well the measured velocity spectra [26, 27]. Therefore, in this study we assume that turbulence follows the von Kármán spectrum.

The streamwise synthetic velocity spectra S_x is defined as

$$S_x = \frac{4L_x\sigma_x}{U_0}\frac{1}{(1+70.7n^2)^{\frac{5}{6}}}, \tag{8}$$

where L_x is the length scale in meters; σ_x is the standard deviation defined as $\sigma_x = I_x U_0$, where I_x is the streamwise turbulent intensity; $n = L_x f_t / U_0$ and f_t is the turbulent frequency component. The velocity spectra in the y-direction is

$$S_y = \frac{4L_y\sigma_y}{U_0}\frac{1+753.6n^2}{(1+282.8n^2)^{\frac{11}{6}}}, \tag{9}$$

where $\sigma_y = R_t\sigma_x$, $L_y = R_t L_x$ and R_t is the anisotropy ratio. For $R_t = 1$, turbulence is isotropic and anisotropic if $R_t < 1$. Here we assume $S_z = S_y$. Velocity time series are simulated using the method of Shinozuka [28]:

$$u_i = \sqrt{2\Delta f_t}\sum_{j=1}^{N}\sqrt{S_{ij}}\cos\Big(2\pi f_{t_j}t + \Phi_j\Big), \tag{10}$$

where i denotes x, y or z; Δf_t is the frequency spacing, N the number of f_t components and Φ is the phase angle, which is a uniformly distributed random variable between 0 and 2π. The velocity time series generated using the Shinozuka method was found to conserve the input standard deviation to the von Kármán spectrum and to be approximately normally distributed.

A range of turbulent parameters, $I_x \in \{5, 20\}$%, $L_x \in \{5, 30\}$ m and $R_t \in \{0.5, 1\}$, are simulated over 50 rotations with $\lambda = 4.5$. From the results shown in Figure 5, it is clear that increasing turbulence intensity elicits the greatest change in $\sigma_{C_{M_y}}$, and that isotropic turbulence produces larger fluctuations than anisotropic turbulence. Decreasing L_x causes a slight increase in $\sigma_{C_{M_y}}$. Notably, there are no isolines showing where the ratio between $\bar{C}_{M_y}$ and $\bar{C}_{M_y(q.s)}$ exceeds unity, which shows that turbulence in isolation does not affect the mean loads for a rotor operating at optimal λ.

C. Wave forcing

A tidal turbine will encounter a large range of waves with varying significant wave height (H_s) and apparent wave period (T_a). In our previous work we considered a measured time series from EMEC during the presence of large waves with $H_s = 5$ m and $T_a = 10$ s [7]. Here we model a range of waves to investigate the effect of amplitude, frequency and direction. We model wave particle velocities using Stokes second-order wave theory for monochromatic waves (see, for instance, Dean and Dalrymple [29]).

A number of waves are simulated with parameters, $H_s \in \{1, 6\}$ m, $T_a \in \{2, 12\}$ s and $\theta \in \{0, 180°\}$. The predicted $\sigma_{C_{M_y}}$ for all flow combinations are shown in Figure 6. We find that the load amplitude is proportional to T_a and, to a lesser extent, H_s. Waves following the tidal current ($\theta = 0$) lead to greater amplitude fluctuations at shorter wave periods, compared to waves opposing the current ($\theta = 180°$). The amplitude is significantly reduced for $\theta = 2\pi/5$ and $3\pi/5$. This is because the perpendicular velocity component becomes small for angles close to $\pi/2$. The isolines show that ratio between $\bar{C}_{M_y}$ and $\bar{C}_{M_y(q.s)}$ only exceeds unity for the most extreme waves.

These results confirm that T_a has more influence on blade loads than H_s and that the load amplitude is increased when waves follow the current.

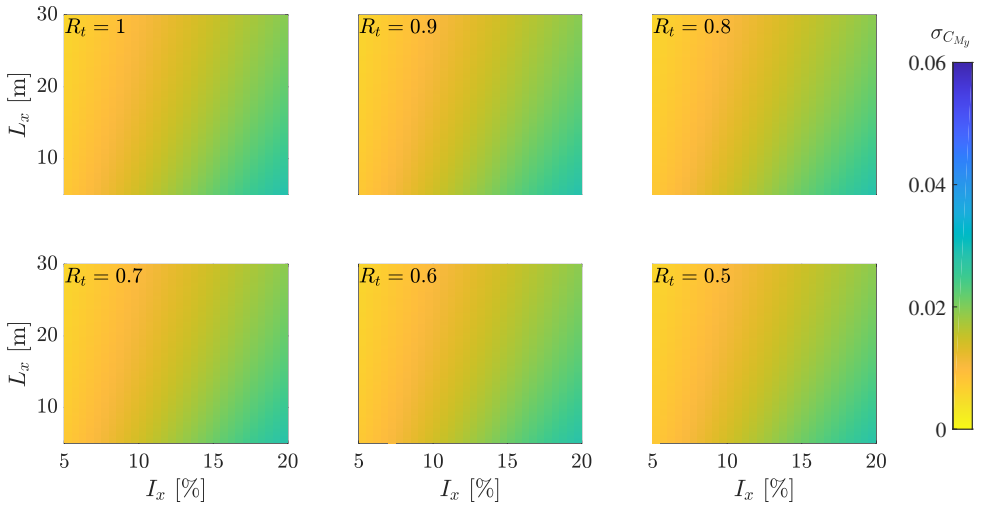

Fig. 5. Filled contour map showing the standard deviation of the root bending moment due to varying turbulence intensity length scale and anisotropy ratio.

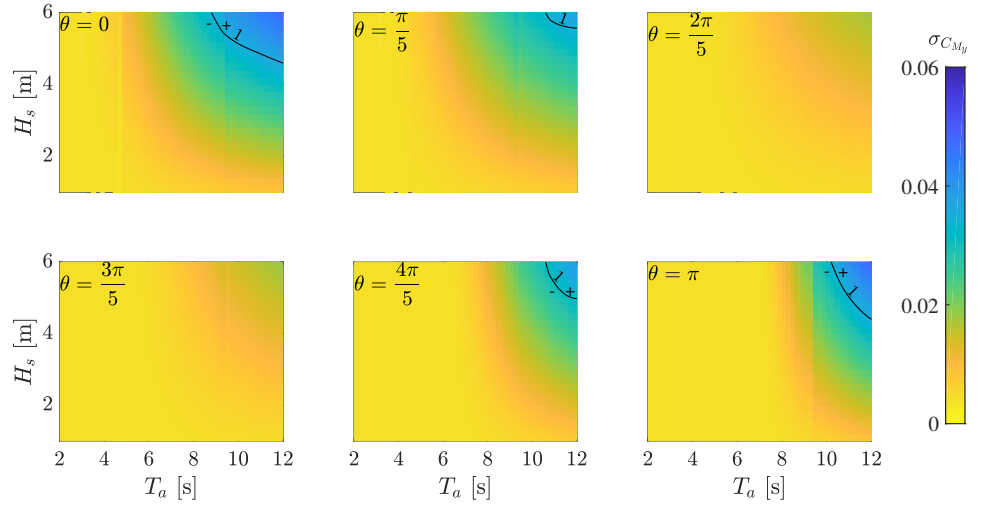

Fig. 6. Filled contour map showing the standard deviation of the root bending moment due to varying wave period, wave height and wave direction. Solid contour lines show the ratio between the mean root bending moment and the quasi-steady counterpart.

D. *Combined forcing*

Combinations of shear, yaw, waves and turbulence are simulated to determine which combined flow condition produces the largest fluctuations. Informed by the results from the individual forcing tests, the flow parameters considered are: isotropic turbulence with $I_x = 0.1$ and $L_x = 20$ m, waves of $H_s = 5$ m, $T_a = 10$ s and $\theta = 0$ and a yaw misalignment of $\gamma = 30°$. The turbine operates at the optimum, $\lambda = 4.5$ and at the velocity for rated power, $U_0 = 2.7$ ms^{-1}. Shear is present for all cases, with $\nu = 1/7$.

A small correction is made to combine the effect of a yawed rotor sampling waves. When this happens, wave particle velocities either lead or lag relative to those experienced at the hub. We use the correction given by Galloway *et al*. [13].

The distribution of C_{M_y} over 100 rotations are presented as a boxplot for each forcing. A boxplot shows the distribution of the quartiles as illustrated in Figure 7. The boxplots for the eight possible flow combinations are shown in Figure 8. As expected, shear in isolation produces the shortest C_{M_y} spread and the inclusion of a yaw misalignment reduces the median value and increases the spread. Turbulence significantly increases the spread and produces some very large outliers. The total spread of C_{M_y} due to waves is shorter than the turbulence case, however, the interquartile range (IQR), containing the 25th to 75th percentiles has the largest spread of the set. Combining waves with turbulence, produces the widest spread in the set (ignoring outliers). The further inclusion of a yaw misalignment with waves and turbulence produces both the minimum and maximum values in the set.

V. *UNSTEADINESS ALONG THE SPAN*

In this section we investigate how unsteadiness unfolds along the blade for different flow combinations and re-

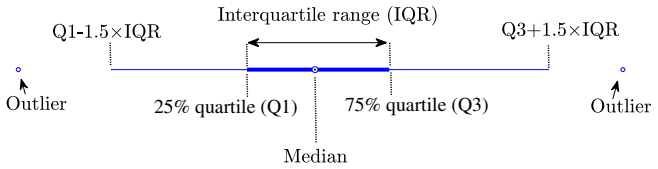

Fig. 7. Box plot descriptor.

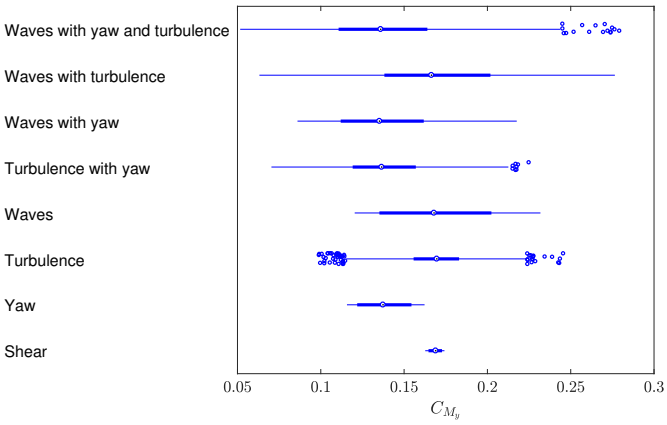

Fig. 8. Box plot showing the summary statistics for the root bending moment time history over 50 blade rotations for several unsteady flow conditions.

veal which unsteady phenomena are occurring.

A. *Unsteady loading from combined flow*

The unsteady response at three span locations, tip ($r = 0.98R$), mid ($r = 0.56R$) and root ($r = 0.15R$), are analysed for each combined flow. Figure 9 shows the distributed thrust force (F_T) at the three blade locations. This force component is responsibly for M_y. The pattern is quite different from C_L. Notably, with dimensions considered, the median value decreases as we travel inboard from tip. The F_T spread is reduced at the root, which is most notable for yawed cases. There is little difference between the spread at the tip and mid sections, since the larger C_L at the mid section counteracts the smaller U_r compared to the tip. The combination of waves with turbulence produces the largest median, peak and widest spread of the set, which, occurs at the mid-section.

B. *Local unsteady characteristics*

Here a visualisation of the unsteady phenomena discussed in section III is given for each of the four flow combinations by displaying on the blade: the location and duration of flow separation, leading edge vortex shedding, highly unsteady regions, where returning wakes are discernible and where added mass is significant. The frequencies used to compute k were determined by analysing the C_L frequency spectrum, whereby the three highest peaks at the tip, mid-section and root of the blade were selected.

The representative blades in Figure 10 show (a) turbulence and yaw, (b) waves and yaw, (c) waves, turbulence and yaw and (d) waves and turbulence. The results reveal that variation in the unsteady phenomena is dependent on the flow forcing. The flow becomes highly unsteady ($k > 0.2$) for every case, however, the transition point on the blade depends on the forcing. For $\gamma = 0$ (d) this occurs at the root of the blade, whereas for turbulence combined with a yaw misalignment, transition occurs outboard of the mid-section. Interestingly, only two of the flow conditions have regions where added mass effects are significant ($k > 0.56$). These are when either turbulence (a) or waves (b) are combined with yaw misalignment. For blade (a) undergoing turbulence and yaw, the affected area is almost a quarter of the span. This case also contains the set maximum $k \approx 0.9$. Compared to blade (b), the affected region is only half the size and confined to the very bottom of the blade where the global effect is negligible due to the low relative velocity and short moment arm. In addition, the flow is separated inside these regions, thus, dynamic stall will govern the loading. Observing separated flow phenomena, it is clear that both regimes of dynamic stall (light and deep) occur on each blade. The blade without a yaw misalignment (d) contains the largest region of flow separation, spanning from the hub to $r \approx 6$ m. Deep dynamic stall, identified by the presence of the LEV, is mostly confined to the blade root. However, for waves with both turbulence and yaw (c) the region covers almost a third of the span.

VI. CONCLUSIONS

In this study we simulated loadings on the blade due to yaw, shear, turbulence and waves to determine which flow conditions induce the most significant load fluctuations on the blade and highlight which unsteady phenomena are occurring.

We showed that turbulence, waves or yaw misalignment can lead to extreme load peaks. Moreover, low tip-speed ratios, as well as large yaw misalignment can cause the mean root bending moment to overshoot the mean value predicted by a quasi-steady approximation. For these reasons it is advisable that unsteady phenomena are always considered in the assessment of both the instantaneous and time-averaged loads on a turbine.

REFERENCES

[1] S. P Neill, A Vögler, A. J Goward-Brown, S Baston, M. J Lewis, P. A Gillibrand, S Waldman, and D. K Woolf. The wave and tidal resource of Scotland. *Renewable Energy*, 114:3–17, 2017.

[2] Meygen LTD. MeyGen Tidal Energy Project Phase 1 Environmental Statement. Technical report, MeyGen, 2012.

[3] L Chen and W.-H Lam. A review of survivability and remedial actions of tidal current turbines. *Re-*

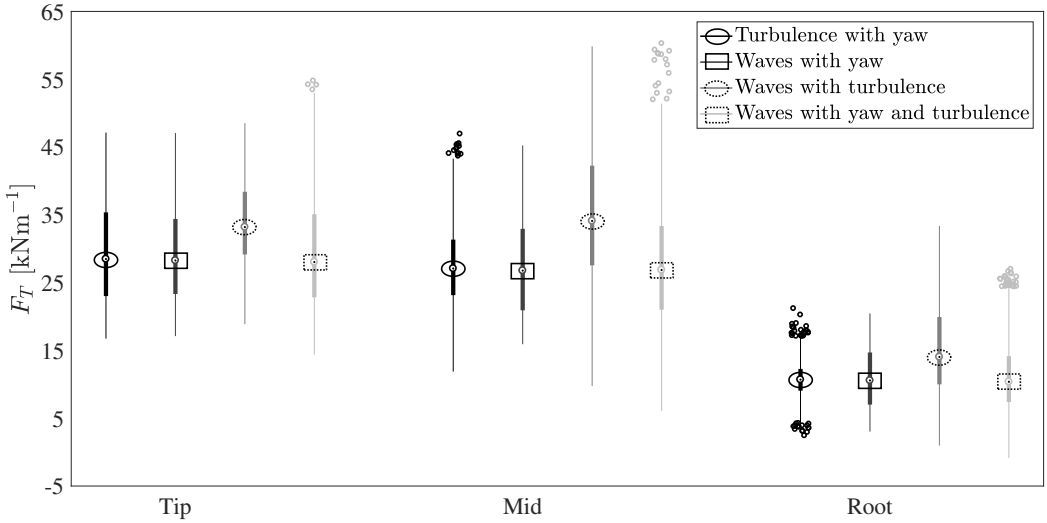

Fig. 9. Box plot showing the summary statistics for the thrust force time history over 50 blade rotations for several unsteady flow conditions at the tip mid and root blade sections.

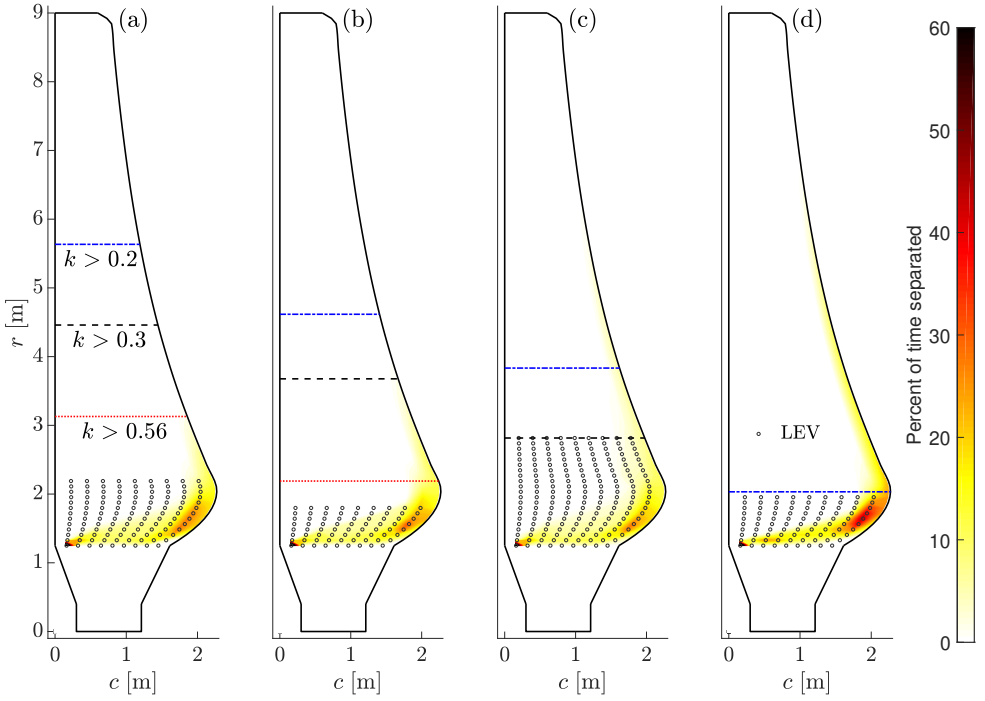

Fig. 10. Parameterisation of unsteady effects along the blade span for, (a) turbulence and yaw, (b) waves and yaw, (c) waves, turbulence and yaw and (d) waves and turbulence.

newable and Sustainable Energy Reviews, 43:891–900, 2015.

[4] D Magagna and A Uihlein. Ocean energy development in Europe: Current status and future perspectives. *International Journal of Marine Energy*, 11:84–104, sep 2015.

[5] W. J McCroskey. Unsteady Airfoils. *Annual Review of Fluid Mechanics*, 14:285–311, 1982.

[6] S Guntur, N. N Sørensen, S Schreck, and L Bergami. Modeling dynamic stall on wind turbine blades under rotationally augmented flow fields. *Wind Energy*, 19(3):383–397, mar 2016.

[7] G. T Scarlett, B Sellar, T van den Bremer, and I. M Viola. Unsteady hydrodynamics of a full-scale tidal turbine operating in large wave conditions. *Renewable Energy*, Submitted, 2018.

[8] J Whelan, J Graham, and J Pierø. Inertia Effects on Horizontal Axis Tidal-Stream Turbines. *Proceedings of the 8th European Wave and Tidal Energy Conference, Uppsala, Sweden*, pages 586–591, 2009.

[9] I. A Milne, A. H Day, R. N Sharma, and R. G. J Flay. Blade loads on tidal turbines in planar oscillatory flow. *Ocean Engineering*, 60:163–174, 2013.

[10] I. A Milne, A. H Day, R. N Sharma, and R. G. J Flay. Blade loading on tidal turbines for uniform unsteady flow. *Renewable Energy*, 77:338–350, 2015.

[11] T Theodorsen. General theory of aerodynamic instability and the mechanism of flutter. *NACA Tech-*

nical Report 496, pages 413 – 433, 1935.

[12] I. A Milne, A. H Day, R. N Sharma, and R. G. J Flay. The characterisation of the hydrodynamic loads on tidal turbines due to turbulence. *Renewable and Sustainable Energy Reviews*, 56:851–864, 2016.

[13] P. W Galloway, L. E Myers, and A. S Bahaj. Quantifying wave and yaw effects on a scale tidal stream turbine. *Renewable Energy*, 63:297–307, 2014.

[14] G. I Gretton. Development of a computational fluid dynamics model for a horizontal axis tidal current turbine. Technical Report WG3 WP5 D1, 2010.

[15] J. G Leishman. *Principles of Helicopter Aerodynamics*. Cambridge University Press, 2006.

[16] D. M McNae. *Unsteady Hydrodynamics of Tidal Stream Turbines*. PhD thesis, Imperial College London, 2013.

[17] G. T Scarlett and I. M Viola. Tidal turbine hydrodynamic model, 2017.

[18] A. S Ning. A simple solution method for the blade element momentum equations with guaranteed convergence. *Wind Energy*, 17:1327–1345, jul 2014.

[19] H Wagner. Über die entstehung des dynamischen auftriebes von tragflügeln. *Journal of Applied Mathematics and Mechanics/Zeitschrift für Angewandte Mathematik und Mechanik*, 5(1):17–35, 1925.

[20] W Sheng, R. A. M Galbraith, and F. N Coton. A new stall-onset criterion for low speed dynamic-stall. *Journal of Solar Energy Engineering*, 128(4):461, 2006.

[21] C Lindenburg. Modelling of rotational augmentation based on engineering considerations and measurements. In *European Wind Energy Conference*, pages 22–25, 2004.

[22] J. M Janiszewska, R Reuss Ramsay, M. J Hoffmann, and G. M Gregorek. Effects of grit roughness and pitch oscillations on the S814 airfoil. Technical report, 1996.

[23] A Ning, G Hayman, R Damiani, and J. M Jonkman. Development and validation of a new blade element momentum skewed-wake model within AeroDyn. In *33rd Wind Energy Symposium*, number December 2014, Reston, Virginia, jan 2015. American Institute of Aeronautics and Astronautics.

[24] T Burton, N Jenkins, D Sharpe, and E Bossanyi. *Wind Energy Handbook*. John Wiley & Sons, Ltd, Chichester, UK, may 2011.

[25] W Diederich, B Franklin, and L Field. Effect of spanwise variations in gust intensity on the lift due to atmospheric turbulence. Technical report, NACA., Langley, 1957.

[26] I. A Milne, R. N Sharma, R. G. J Flay, and S Bickerton. Characteristics of the turbulence in the flow at a tidal stream power site. *Philosophical Transactions of the Royal Society A: Mathematical, Physical and Engineering Sciences*, 371(1985):20120196, 2013.

[27] I. A Milne, R. N Sharma, and R. G. J Flay. The structure of turbulence in a rapid tidal flow. *Proceedings of the Royal Society A: Mathematical, Physical and Engineering Science*, 473(2204):20170295, aug 2017.

[28] M Shinozuka. Monte Carlo solution of structural dynamics. *Computers and Structures*, 2(5-6):855–874, 1972.

[29] R. G Dean and R. A Dalrymple. *Water Wave Mechanics for Engineers and Scientists*, volume 2 of *Advanced Series on Ocean Engineering*. World Scientific Publishing Co. Pte. Ltd., 1991.